A high power, high density helicon discharge for the plasma wakefield accelerator experiment AWAKE

B. Buttenschön,[1] N. Fahrenkamp,[1] and O. Grulke[1]

Max Planck Institute for Plasma Physics, Wendelsteinstr. 1, 17491 Greifswald, Germany

A plasma cell prototype for the plasma wakefield accelerator experiment AWAKE based on a helicon discharge is presented. In the one meter long prototype module a multiple antenna helicon discharge with an rf power density of $100\,\mathrm{MW/m^3}$ is established. Based on the helicon dispersion relation, a linear scaling of plasma density with magnetic field is observed for rf frequencies above the lower hybrid frequency, $\omega_{\mathrm{LH}} \leq 0.8\omega_{\mathrm{rf}}$. Density profiles are highest on the device axis and show shallow radial gradients, thus providing a relatively constant plasma density in the center over a radial range of $\Delta r \approx 10\,\mathrm{mm}$ with less than 10% variation. Peak plasma densities up to $7 \cdot 10^{20}\,\mathrm{m^{-3}}$ are transiently achieved with a reproducibility that is sufficient for AWAKE. The results are in good agreement with power balance calculations.

I. INTRODUCTION

There is an interdisciplinary need for unconfined high density plasmas for scientific as well as industrial research and development purposes. Great efforts are made at the link between fusion research and material sciences, the investigation of plasma-wall interactions, to find materials suitable for use in the high heat and particle flux region of the divertor in future fusion devices. A number of machines with different plasma sources are dedicated to this topic: experiments like Magnum-PSI[1,2] or PISCES[3,4] use (cascaded) arc discharges as sources for high density plasmas, while MAGPIE[5] or the Oak Ridge National Laboratory's high particle flux plasma source[6,7] employ helicon discharges to create high density plasmas. All these experiments reach plasma densities on the order $n_e = (10^{19} \dots 10^{20})\,\mathrm{m}^{-3}$ at electron temperatures below $T_e = 10\,\mathrm{eV}$. In the last 15 years, a number of experiments aiming at electric propulsion concepts for spacecraft engines emerged[8]. Two prominent examples for ongoing studies include the VASIMR™ concept[9–11] and the High Power Helicon Thruster[12,13], both using a helicon source for the creation of the initial high density plasma. Again, the plasma densities in these prototype thrusters reach values $n_e < 10^{20}\,\mathrm{m}^{-3}$.

Since the proposal of the plasma wakefield accelerator (PWA) concept[14], high density plasmas are of interest also in the context of advanced plasma-based accelerators. For PWAs, a long homogeneous high-density plasma column is required to create and maintain high accelerating electric fields of the order GV/m. In these fields, particles can be accelerated to energies in the TeV range in comparatively short accelerators. The largest accelerating fields in PWA to date, which are of the order 100 GV/m, have been obtained using laser-ionized metal vapor plasmas in centimeter-scale accelerators[15,16]. The concept of particle-driven PWA[17–20] has been proven by the energy doubling of 42 GeV electrons to more than 80 GeV within an accelerator length of only 85 cm[21]. Current PWA experiments, however, lack scalability to much longer device lengths and therefore need a staged set-up in order to achieve high output energies.

In this work, we present a high power helicon plasma source capable of creating electron densities relevant for PWA construction. Although this experiment is principally designed for and dedicated to plasma wakefield accelerator development, a plasma source like this is also beneficial to plasma wall interaction or spacecraft thruster studies. The design and construction of this experiment is embedded in an international effort to build the first

experiment worldwide on proton-driven plasma wakefield acceleration, the Advanced Wakefield Experiment AWAKE[22,23]. The PWA concept of using a proton beam as wakefield driver was only recently proposed[24]. Simulations indicate that accelerating fields of typically $E_z = (2 \ldots 3)\,\mathrm{GV/m}$ can be achieved using a short proton bunch as wakefield driver[24,25]. The device presented in this work is dedicated to demonstrate that the target density for the AWAKE experiment, $n_e = 7 \cdot 10^{20}\ \mathrm{m}^{-3}$, can be achieved by means of a high power helicon discharge, which is intrinsically scalable in length and can thus avoid the necessity for staging.

II. BASIC POWER BALANCE

Regardless of the actual heating scheme, the power required to maintain a plasma discharge of a given density can be estimated considering the general power and particle balance of the discharge. Figure 1 shows the result of calculations for three different rf heating powers, each with an initial neutral gas (argon) fill pressure of $p_0 = 5$ Pa, a length of 1 m and an effective plasma radius of 10 mm. Electron density and temperature are assumed constant throughout the discharge volume. The power and particle balance scheme used for this work[26] balances the rf input power with all relevant sources and sinks: ionization, excitation, recombination, coulomb collisions between electrons and ions, as well as particle losses to the vessel walls. The results of this balance clearly show the need for a low temperature discharge. Figure 1b shows a power requirement of $P_{\mathrm{rf}} \approx 25\,\mathrm{kW}$ to produce the nominal plasma density of $n = 7 \cdot 10^{20}\,\mathrm{m}^{-3}$ at an electron temperature of $T_{\mathrm{e}} = 1.5\,\mathrm{eV}$, increasing to $P_{\mathrm{rf}} \approx 88\,\mathrm{kW}$ at $T_{\mathrm{e}} = 2.0\,\mathrm{eV}$ and $P_{\mathrm{rf}} \approx 300\,\mathrm{kW}$ at $T_{\mathrm{e}} = 2.5\,\mathrm{eV}$.

Based on these considerations, a helicon wave heated discharge seems to be a suitable choice. Although the exact process of energy dissipation from the wave to the plasma is still under debate[27–33], helicon discharges are long known for their very efficient plasma production[34,35] due to the non-resonant nature of the rf power dissipation via collisional damping, providing only small electron temperatures in favor of high density generation. Helicon discharges have been demonstrated to routinely produce plasma densities around $n_e \approx 10^{20}\,\mathrm{m}^{-3}$ at moderate rf heating power densities of up to a few $\mathrm{MW/m^3}$,[36–46] and have already been proposed to be used as high density plasma source for particle accelerators[47]. The heating by external antennas and the centrally peaked density profile[35,46,48,49] make

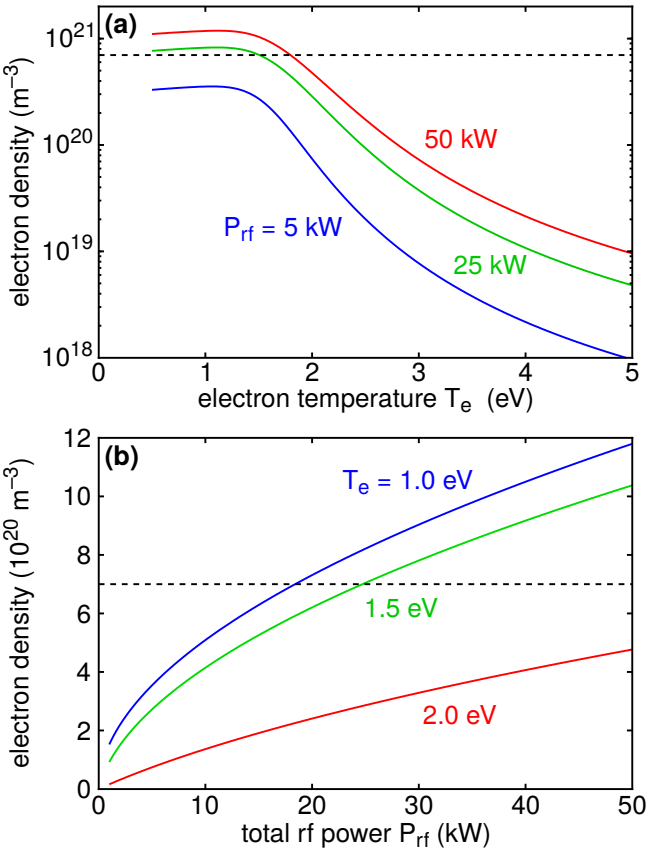

FIG. 1. Results of a power and particle balance for an argon discharge. The black dashed line marks the AWAKE nominal density of $n_e = 7 \cdot 10^{20}$ m^{-3}, which is reached only at electron temperatures below 2 eV for reasonable rf power levels. (a) Density variation over electron temperature. (b) Density variation over injected heating power.

helicon wave heated discharges an ideal choice for the plasma cell of a PWA. However, plasma densities significantly beyond a value of $n_e = 1 \cdot 10^{20}\,\mathrm{m}^{-3}$ have not yet been reported. The density limit observed in different experiments is commonly attributed to neutral pumping, where the neutral gas in the discharge center is depleted by ions leaving the discharge axially with Bohm speed, while thermal neutrals cannot penetrate the plasma center due to short mean free paths for ionization[37,50,51]. In this work, we describe a high power helicon plasma source in which central electron densities $n_e > 6.5 \cdot 10^{20}\,\mathrm{m}^{-3}$ are transiently achieved on time scales suitable for PWA purposes, demonstrating the general suitability of helicon discharges for future particle accelerator applications.

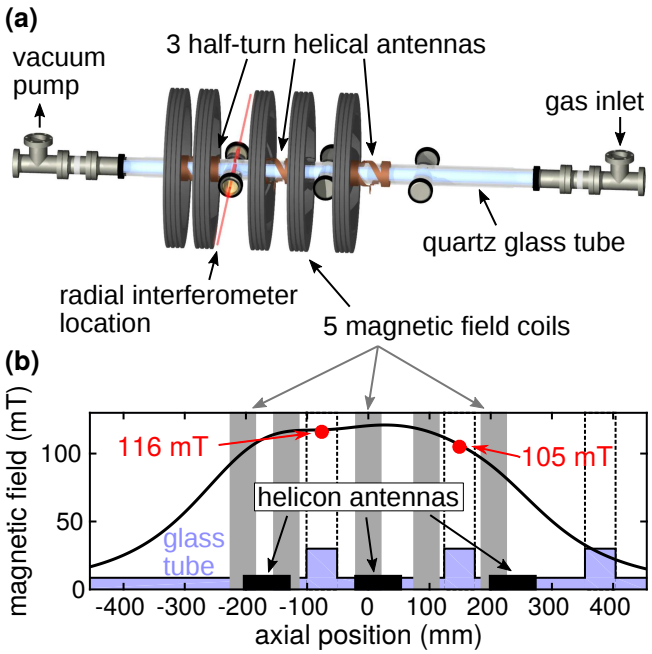

FIG. 2. (a) The 1 meter long prototype module PROMETHEUS-A for the plasma wakefield accelerator experiment AWAKE. The magnetic field coils are adjusted to produce a field as homogeneous as possible, while providing access to the radial ports of the tube for diagnostic purposes. The interferometer position at the leftmost port is marked by a red beam. (b) Calculated magnetic field on axis for the highest available coil current. Measured values at two ports are shown as red dots.

III. EXPERIMENTAL SETUP

A schematic drawing of the experiment PROMETHEUS-A, the **Pro**totype **M**odule for **E**xperimen**t**s on High Power **He**licons as **U**niform Plasma **S**ource for **A**WAKE, is shown in Fig. 2a. It consists of a one meter long quartz glass tube with 50 mm outer diameter (44 mm inner), along which three identical $m = +1$ half-turn helical antennas ($l_{\mathrm{ant}} = 75\,\mathrm{mm}$) are equidistantly placed. Each of the antennas is fed by an identical chain of rf generator and manual L-type capacitive matching circuit. With each rf generator supplying up to $P_{\mathrm{rf}} = 12\,\mathrm{kW}$, a total power of typically $P_{\mathrm{rf}} \leq 27\,\mathrm{kW}$ can be delivered into the system without arcing at the antennas. The axial magnetic field required for helicon wave excitation is created by five water-cooled copper coils, providing an on-axis magnetic field up to $B_z \leq 116\,\mathrm{mT}$ for coil currents $I_{\mathrm{coil}} \leq 370\,\mathrm{A}$ as shown in Fig. 2b. The working gas, typically argon, is continuously pumped at one axial end and fed into the system at the opposite axial end of

the discharge tube. For the presented measurements, no gas flow control or pump limitation was implemented, but the gas flow was manually adjusted at the inlet side for a constant fill pressure in the range $p_0 = (3 \ldots 15)\,\mathrm{Pa}$. The discharge is operated in a pulsed mode with $f = 10\,\mathrm{Hz}$ and 10% duty cycle to generate fast ($\approx \mu$s) ramp-ups of the rf power while reducing the heat load on the glass tube and antennas during high power operation.

Chief diagnostic tool is a 2-pass CO_2 laser interferometer ($\lambda = 10.6\,\mu\mathrm{m}$) measuring the radially line-integrated plasma density at one axial location between two helicon antennas (see Fig. 2). The complete plasma cell is mounted on four electric lifting cylinders and can be vertically moved with respect to the laser interferometer. This allows to measure the line-integrated radial density profile on a pule-to-pulse basis, which in turn is used to derive the radial density profile at the location of the interferometer measurement assuming azimuthal symmetry of the discharge.

An important parameter for the use in PWA applications is the axial density homogeneity. While no diagnostic means are installed at PROMETHEUS-A to assess the axial density distribution and thus no measurements are available, global density gradients along the axis are unlikely due to the evenly distributed power coupling with each antenna providing the same amount of rf heating power to the plasma. Possible inhomogeneities in the regions between the antennas are thought to be controllable by adjusting the antenna spacing and the local magnetic field. The investigation of the effectiveness of these control parameters remains an open task until the diagnostic possibilities are extended.

IV. RESULTS

A. Time-resolved density evolution

The evolution of the plasma density follows a very similar form for all operating parameters. Figure 3 shows the first 1 ms of a number of measurements at different rf power levels. Each of the lines represents the average time trace of typically 10 individual discharges. The error bars indicate the total variation of measured densities for $P_{\mathrm{rf}} = 4.5\,\mathrm{kW}$ and $P_{\mathrm{rf}} = 27\,\mathrm{kW}$. For all rf power levels, the plasma density quickly rises to a peak value within a few $100\,\mu$s and decreases to some steady-state density within the following 2 ms. One could speculate that this temporal variation of the plasma density is related to the

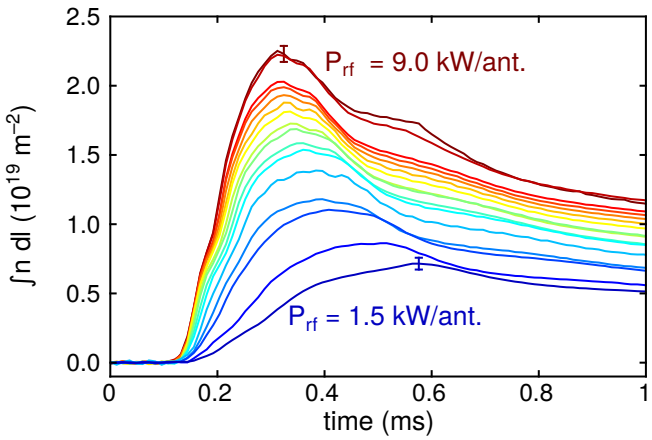

FIG. 3. Evolution of line-integrated electron density within the first 1 ms of an rf pulse. Lines correspond to different rf power levels between 4.5 kW and 27 kW. The error bars indicate the total variation of the density in the vicinity of the indicated time step over typically 10 discharges.

neutral gas fueling, the so-called neutral pumping effect[51–54]. This aspect is subject to further investigations. However, the reproducibility of the peak density occurrence, which is important for PWA purposes, can already be assessed.

In figure 4, the time of the peak density t_{peak} is shown along with the peak width w_{98}, defined as the time in which the density is higher than 98% of the peak density, for the same set of discharges as in Fig. 3. Each point corresponds to one singe plasma discharge, with the rf power level color coded. The dashed lines indicate those discharges with $P_{\mathrm{rf}} \geq 25.5\,\mathrm{kW}$; the values given for t_{peak} and w_{98} correspond to that set of discharges. With a peak density occurrence at $t_{\mathrm{peak}} = (241 \pm 10)\,\mu\mathrm{s}$, the jitter is much smaller than $w_{98} = (64 \pm 5)\,\mu\mathrm{s}$. For PWA usage, where relativistic particle beams with $v \approx c$ pass a 1 km long plasma cell in less than $5\,\mu\mathrm{s}$, the density peak timing stability shown here is absolutely sufficient for this application.

B. Influence of operational parameters on the radial density profile

In order to calculate absolute plasma densities from the line-integrated interferometer measurement, knowledge of the radial plasma density profile is crucial. Figures 5, 6 and 7 show the line-integrated measured density profiles recorded over the full range of the experiment's operational parameters. In all cases, the profile is centrally peaked and generally

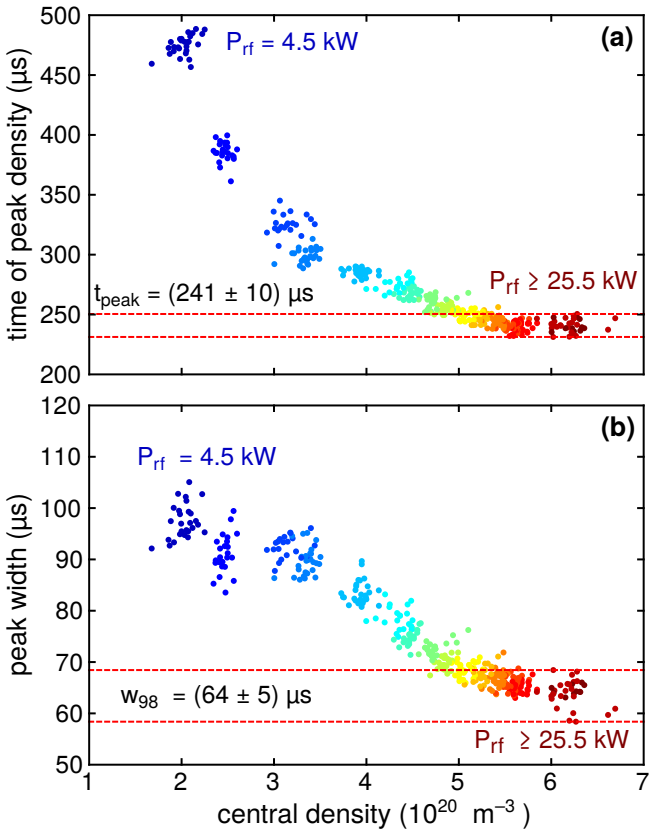

FIG. 4. Peak density characteristics. (a) Time of peak occurrence, (b) Width of region where $n_e > 0.98 \cdot n_{e,\mathrm{peak}}$. The given numbers relate to measurements with $P_{\mathrm{rf}} \geq 25.5\,\mathrm{kW}$, the timing errors are the maximum deviations from the average timing and width.

follows a parabolic shape. Each profile is fitted by a function $n(r)/n_0 = 1 - (|r|/w)^s$ with the central density n_0, radial position r, the total profile width w with $n(w) = 0$, and a shape parameter s. The width w and parameter s are free fit parameters. As reference case, which is used for standard density evaluation, we use a parabolic profile with $w = 22\,\mathrm{mm}$ and $s = 2$.

Since in some cases only a small number (< 10) of discharges is available for evaluation per profile position, the error bars in figures 5, 6 and 7 indicate the highest deviation from the mean value measured in the available discharges at that position. Identifying residual noise on the interferometer signal as the main source of error (introducing an uncertainty of $n_e \approx 1 \cdot 10^{18}\,\mathrm{m}^{-2}$), the relative errors decrease with increasing absolute density (i.e. towards higher power, higher field, and higher pressure) and reach values below 5 % at highest densities.

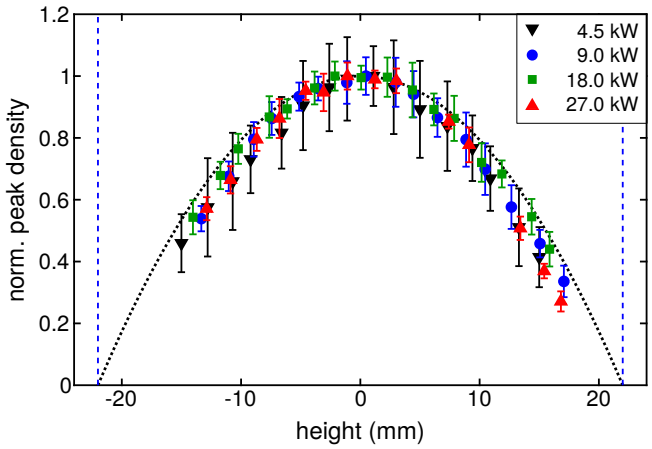

FIG. 5. Normalized line-integrated density profiles for $p_0 = 5\,\mathrm{Pa}$, $B_z = 116\,\mathrm{mT}$ and varying applied rf power levels. The profile shape is not changed over a wide range of rf power levels, but remains in its generic parabolic shape (black dotted line). The blue dashed lines indicate the position of the inner wall of the discharge tube.

Keeping fill pressure and axial magnetic field strength constant while varying the applied rf power (Fig. 5), the measured profiles do not change over the full range of rf power levels and stay close to the reference case shown by the dotted line. In all cases, the measured line-integrated densities even stay below the reference, thus slightly underestimating the absolute density in the standard evaluation procedure assuming a parabolic profile.

Figure 6 shows the profiles for various axial magnetic field strengths at two different rf power levels, $P_{\mathrm{rf,set}} = 15\,\mathrm{kW}$ (a) and $P_{\mathrm{rf,set}} = 27\,\mathrm{kW}$ (b), while the neutral gas fill pressure is kept constant. Again, the overall profile shape does not deviate significantly from the generic parabola shown as black dotted line. However, a trend to narrower profiles is observed with increased magnetic field strength for both rf power levels. This behavior can be attributed to a reduced radial transport of ions at higher magnetic fields: the ion gyro radius (for singly ionized argon at room temperature) decreases from $r_{\mathrm{ci}}(30\,\mathrm{mT}) = 4.9\,\mathrm{mm}$ to $r_{\mathrm{ci}}(116\,\mathrm{mT}) = 1.3\,\mathrm{mm}$. Especially for the high power case, this profile change leads to a slight overestimation of absolute densities at low magnetic field and underestimation at high field strength when using the standard inversion with a parabolic profile.

The influence of the initial fill pressure on the density profile is shown in Fig. 7. Here, the axial magnetic field strength is kept constant and profiles are measured for the same two rf power levels as before. In the low power case (top panel), there are no large deviations of

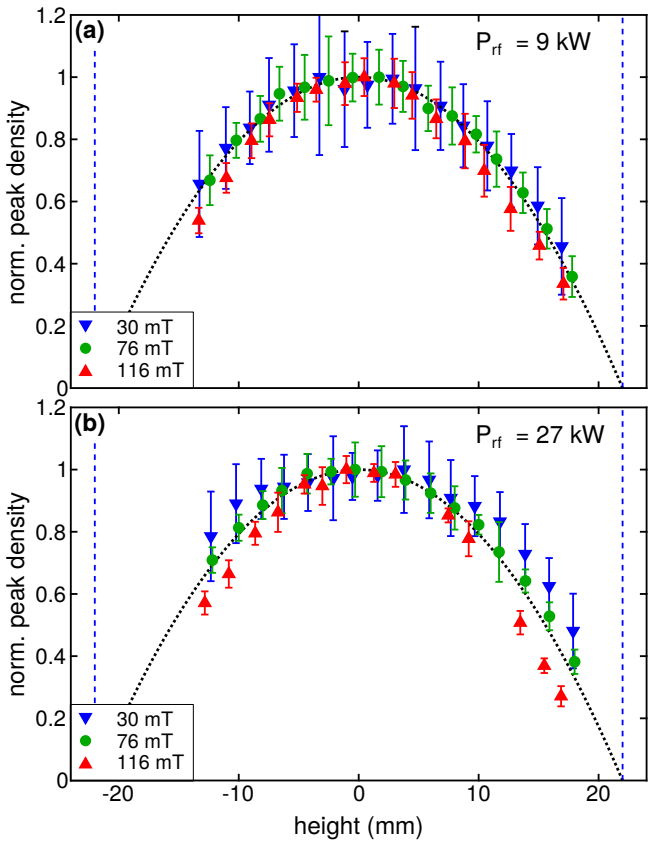

FIG. 6. Normalized line-integrated density profiles for $p_0 = 5\,\mathrm{Pa}$ and varying applied magnetic field. (a) $P_{\mathrm{rf,set}} = 15\,\mathrm{kW}$ (b) $P_{\mathrm{rf,set}} = 27\,\mathrm{kW}$. The generic parabolic profile is indicated by the black dotted line. Especially for the high rf power case a significant change of the profile shape is observed, with narrower profiles at higher magnetic field strengths.

the measured profiles from the generic parabolic shape, with only a slight profile broadening towards higher fill pressures. There is, however, a significant influence on the profile shape in the high power case (bottom panel). Here, the line-integrated densities stay below the reference case at all radii for pressures up to $p_0 = 5\,\mathrm{Pa}$, while for pressures larger than $p_0 = 8\,\mathrm{Pa}$ a significant broadening of the profiles is observed. For $p_0 = 15\,\mathrm{Pa}$, the measured line-integrated density profile even shows a clear dip in the plasma center, which might indicate significant rf power absorption in the plasma edge due to inductive heating effects. With these large deviations from the model profile, we constrain ourselves in the following to fill pressures $p_0 \leq 8\,\mathrm{Pa}$, where the profile inversion using the parabolic model is still valid.

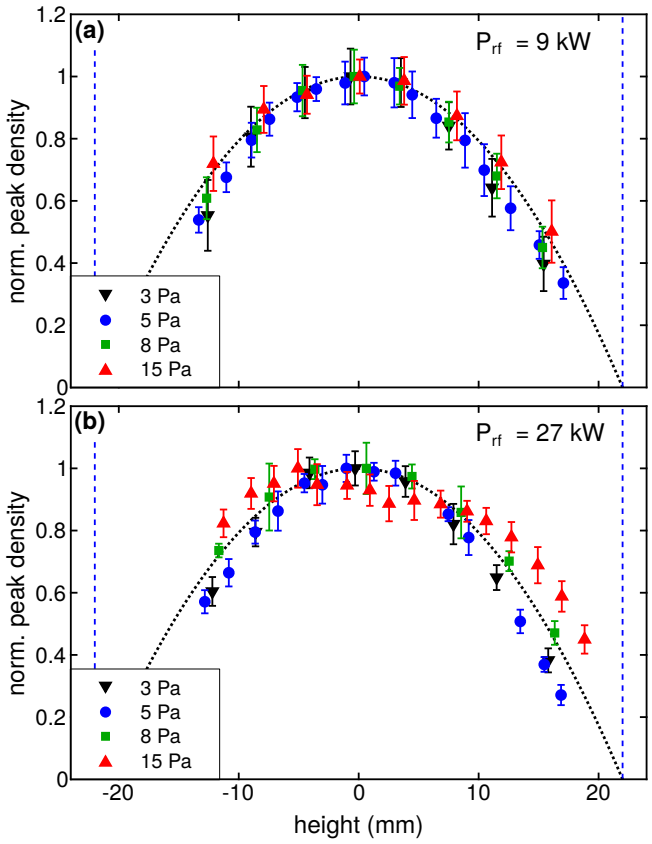

FIG. 7. Normalized line-integrated density profiles for $B_z = 116\,\mathrm{mT}$ and varying initial fill pressure. (a) $P_{\mathrm{rf,set}} = 15\,\mathrm{kW}$ (b) $P_{\mathrm{rf,set}} = 27\,\mathrm{kW}$. The generic parabolic profile is indicated by the black dotted line. The profile broadens with increasing fill pressure, and even dips in the center for high power and high pressure.

C. Peak density scaling compared to models

Using the observed stiffness of the radial density profile shape over a wide range of operational parameters, we can invert the measured line-integrated densities to retrieve radially resolved local densities, assuming that the parabolic profile is valid for all variations of $P_{\mathrm{rf,set}}$ and B_z. The Abel-inversion of a parabolic line-integrated profile yields a local density profile of the form $n(r) \propto \sqrt{R^2 - r^2}$, which is used to transform the line-integrated density into local values for all following considerations. The so obtained local density values can now be compared to what models would predict for the given operation parameters of the helicon discharge.

The (simplified) dispersion relation of a helicon wave reads[27] $k_\parallel k/\omega = n_e e \mu_0 / B_z$ with a

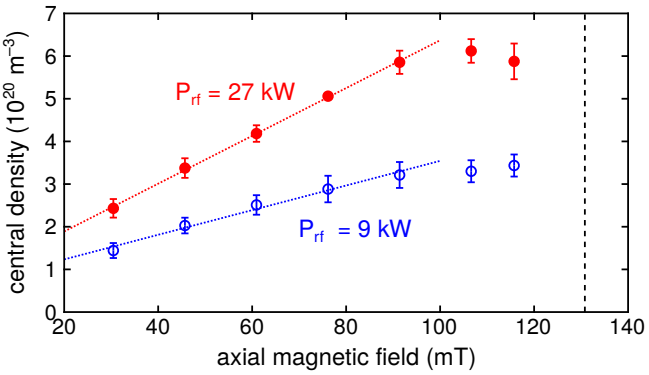

FIG. 8. Scaling of the central electron density with magnetic field strength for two different rf power levels. The black dashed line indicates the magnetic field $B_z = 130.8\,\mathrm{mT}$ at which the lower hybrid frequency matches the rf frequency of 13.56 MHz at an electron density $n_e = 6 \cdot 10^{20}\,\mathrm{m}^{-3}$. Data are taken at $p_0 = 5\,\mathrm{Pa}$ and $B_z = 116\,\mathrm{mT}$.

driving frequency $\omega_{\mathrm{rf}} = 2\pi \times 13.56\,\mathrm{MHz}$ in the present case. Assuming that the parallel and perpendicular wave numbers $k_\perp$ and $k_\parallel$ are fixed by the experiment and antenna geometry, this introduces a linear dependence of the plasma density on the magnetic field strength which is valid if $\omega_{\mathrm{LH}} < \omega_{\mathrm{rf}}$ with the lower hybrid frequency ω_{LH}[55]. Figure 8 shows the scaling of the peak density (i.e. in the axial center of the inverted profile) with the applied axial magnetic field strength for two different power levels of $P_{\mathrm{rf,set}} = 9\,\mathrm{kW}$ and $P_{\mathrm{rf,set}} = 27\,\mathrm{kW}$, along with a linear fit to the data for magnetic field strengths $B_z < 100\,\mathrm{mT}$ to illustrate the linear scaling behavior. At magnetic field strengths closer to the value where the lower hybrid frequency matches the rf driving frequency (indicated by the black dashed line), the linear trend does not continue and the density increases slower than expected from the dispersion, or even starts to decrease. Since external operation parameters (e.g. the rf load power) can be excluded to be causing this decrease, the observed behavior hints towards the decrease of heating efficiency due to the change of coupling between the helicon and Trivelpiece-Gould wave close to the lower hybrid frequency, which has been observed both numerically and experimentally[33,45,56].

Following the power balance scheme from section II, the central plasma density should be monotonically increasing with applied rf power. A comparison between the output of the power balance (using a neutral gas pressure of $p_0 = 5\,\mathrm{Pa}$ and a 10 mm wide flat-top density profile) and measured central density is show in Fig. 9. The rf power values given here

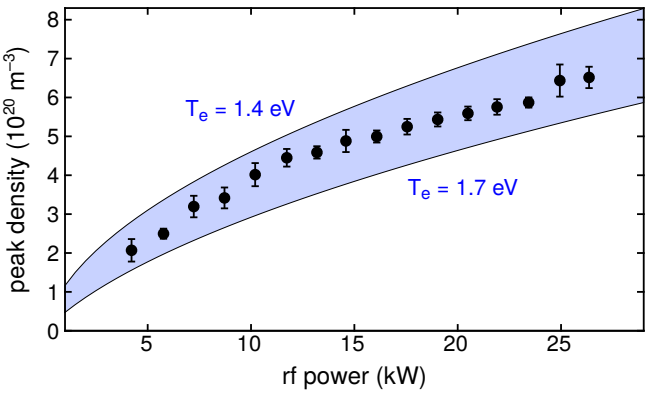

FIG. 9. Scaling of the central electron density with total rf power. The shaded area indicates the density region the power balance predicts for an initial gas pressure of $p_0 = 5\,\mathrm{Pa}$ and a flat-top density profile with 10 mm radius within the boundary of the electron temperature values shown.

are the total load power measured by the rf generators. The measured data show the same general trend as the power balance and, within the error bars of the measurement, the match the power balance calculation in a temperature range $T_e = (1.4 \ldots 1.7)\,\mathrm{eV}$. The low electron temperature obtained from this comparison is consistent with the heating mechanism of helicon waves via collisional wave power dissipation.

D. Peak density at optimal parameters

Combining the findings of the parameter scans, an optimized set of operation parameters is determined and expected to yield the highest achievable plasma density using the presented set-up. This set of parameters uses the highest available rf power ($P_{\mathrm{rf,set}} = 27\,\mathrm{kW}$), a magnetic field strength for which the lower hybrid frequency is far enough from the rf driving frequency ($B_z = 106\,\mathrm{mT}$) and a neutral gas pressure for which the density profile is still centrally peaked ($p_0 = 8\,\mathrm{Pa}$). Figure 10 shows the measured inverted density profile for this set of operation parameters, along with the inverted model function. The measured densities reach $n_{e,\mathrm{meas}} = (6.96 \pm 0.38) \cdot 10^{20}\ \mathrm{m}^{-3}$, while the fitted model function yields a central density of $n_{e,\mathrm{model}} = 6.83 \cdot 10^{20}\ \mathrm{m}^{-3}$. The AWAKE design density of $7 \cdot 10^{20}\ \mathrm{m}^{-3}$ is therefore achievable with the given operational parameters, with the innermost 10 mm of the plasma radius still exceeding a value of $6.5 \cdot 10^{20}\ \mathrm{m}^{-3}$.

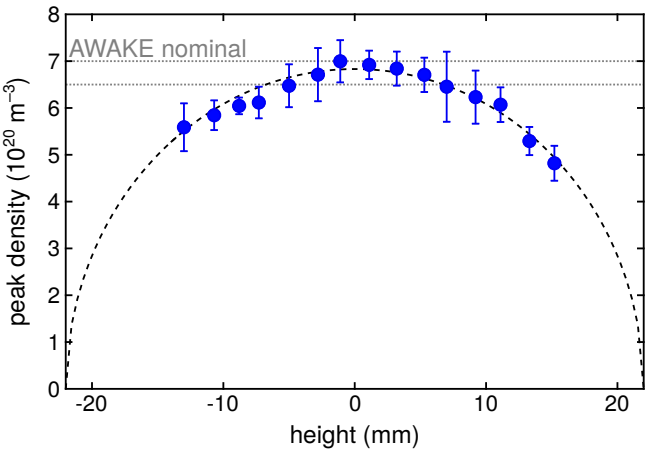

FIG. 10. Density profile at $p_0 = 5\,\mathrm{Pa}$, $B_z = 106\,\mathrm{mT}$, and $P_{\mathrm{rf,set}} = 27\,\mathrm{kW}$. Blue dots are measured values mapped to local densities using the parabolic model function for line-integrated values. The black dashed line marks the inverted model function, and the gray dotted lines mark the design density, $n_e = 7 \cdot 10^{20}\,\mathrm{m}^{-3}$, and a slightly lower density of $n_e = 6.5 \cdot 10^{20}\,\mathrm{m}^{-3}$, which is exceeded by the inner 10 mm of the plasma radius.

V. SUMMARY AND CONCLUSIONS

In the new high-power, high-density helicon discharge PROMETHEUS-A, plasma densities up to $n_e \approx 7 \cdot 10^{20}\,\mathrm{m}^{-3}$ have to our knowledge been achieved for the first time in a helicon discharge. The rf heating power needed to reach this density is in good agreement with a power and particle balance calculation, which yields low electron temperatures around $T_e = 1.5\,\mathrm{eV}$ when compared with measurements. Scans of the operational parameters, which are the neutral gas fill pressure, the magnetic field strength and the rf power fed into the system, show a robust shape of the radial plasma density profile. A significant deviation from a centrally peaked profile is observed only at very high neutral gas pressures, while a variation of the remaining operational parameters lead to only slight variations in the width of the profile. The time-resolved density evolution in this experiment shows a distinct peak of the density within the first few $100\,\mu\mathrm{s}$, with a jitter well below the width of the peak where the density exceeds 98 % of the peak density value. In combination with the modular approach towards a scalable plasma source that PROMETHEUS-A is based on, the measured profiles, densities and timing properties make this helicon plasma source a suitable choice for the next stage of the AWAKE plasma wakefield accelerator.

ACKNOWLEDGMENTS

This work has been carried out within the framework of the AWAKE Collaboration. The authors thank all collaboration members for discussion and support.

REFERENCES

[1]J. Rapp, W. R. Koppers, H. J. N. van Eck, G. J. van Rooij, W. J. Goedheer, B. de Groot, R. Al, M. F. Graswinckel, M. A. van den Berg, O. Kruyt, P. Smeets, H. J. van der Meiden, W. Vijvers, J. Scholten, M. van de Pol, S. Brons, W. Melissen, T. van der Grift, R. Koch, B. Schweer, U. Samm, V. Philipps, R. A. H. Engeln, D. C. Schram, N. J. L. Cardozo, and A. W. Kleyn, Fusion Eng. Des. **85**, 1455 (2010).

[2]H. J. N. van Eck, T. Abrams, M. A. van den Berg, S. Brons, G. G. van Eden, M. A. Jaworski, R. Kaita, H. J. van der Meiden, T. W. Morgan, M. J. van de Pol, J. Scholten, P. H. M. Smeets, G. D. Temmerman, P. C. de Vries, and P. A. Z. van Emmichoven, Fusion Eng. Des. **89**, 2150 (2014).

[3]D. M. Goebel, G. Campbell, and R. W. Conn, J Nucl Mater **121**, 277 (1984).

[4]R. P. Doerner, M. J. Baldwin, R. W. Conn, A. A. Grossman, S. C. Luckhardt, R. Seraydarian, G. R. Tynan, and D. G. Whyte, J Nucl Mater **290–293**, 166 (2001).

[5]B. D. Blackwell, J. F. Caneses, C. M. Samuell, J. Wach, J. Howard, and C. Corr, Plasma Sources Sci Technol **21**, 055033 (2012).

[6]R. H. Goulding, T. M. Biewer, J. B. O. Caughman, G. C. Chen, L. W. Owen, and D. O. Sparks, AIP Conf Proc **1406**, 535 (2011).

[7]J. Rapp, T. M. Biewer, J. Canik, J. B. Caughman, G. Chen, S. J. Diem, R. H. Goulding, D. L. Hillis, J. D. Lore, A. Lumsdaine, W. D. McGinnis, S. J. Meitner, L. Owen, Y. K. M. Peng, and S. L. Milora, Proc. 24textsuperscriptth IAEA Fusion Energy Conf. , FTP/P1-33 (2012).

[8]E. Ahedo, Plasma Phys Control Fusion **53**, 124037 (2011).

[9]F. R. Chang Díaz, Sci Amer **283**, 90 (2000).

[10]F. R. Chang Díaz, AIP Conference Proceedings **595**, 3 (2001).

[11]A. V. Arefiev and B. N. Breizman, Phys Plasmas **11**, 2942 (2004).

[12]T. Ziemba, P. Euripides, J. Slough, R. Winglee, L. Giersch, J. Carscadden, T. Schnackenberg, and S. Isley, Plasma Sources Sci. Technol. **15**, 517 (2006).

[13]R. Winglee, T. Ziemba, L. Giersch, J. Prager, J. Carscadden, and B. R. Roberson, Phys Plasmas **14**, 063501 (2007).

[14]T. Tajima and J. M. Dawson, Phys. Rev. Lett. **43**, 267 (1979).

[15]M. J. Hogan, C. D. Barnes, C. E. Clayton, F. J. Decker, S. Deng, P. Emma, C. Huang, R. H. Iverson, D. K. Johnson, C. Joshi, T. Katsouleas, P. Krejcik, W. Lu, K. A. Marsh, W. B. Mori, P. Muggli, C. L. O'Connell, E. Oz, R. H. Siemann, and D. Walz, Phys. Rev. Lett. **95**, 054802 (2005).

[16]W. P. Leemans, B. Nagler, A. J. Gonsalves, C. Tóth, K. Nakamura, C. G. R. Geddes, E. Esarey, C. B. Schroeder, and S. M. Hooker, Nat Phys **2**, 696 (2006).

[17]P. Chen, J. M. Dawson, R. W. Huff, and T. Katsouleas, Phys Rev Lett **54**, 693 (1985).

[18]P. Chen, J. M. Dawson, R. W. Huff, and T. Katsouleas, Phys Rev Lett **55**, 1537 (1985).

[19]P. Muggli, B. E. Blue, C. E. Clayton, S. Deng, F.-J. Decker, M. J. Hogan, C. Huang, R. Iverson, C. Joshi, T. C. Katsouleas, S. Lee, W. Lu, K. A. Marsh, W. B. Mori, C. L. O'Connell, P. Raimondi, R. Siemann, and D. Walz, Phys. Rev. Lett. **93**, 014802 (2004).

[20]M. Litos, E. Adli, W. An, C. I. Clarke, C. E. Clayton, S. Corde, J. P. Delahaye, R. J. England, A. S. Fisher, J. Frederico, S. Gessner, S. Z. Green, M. J. Hogan, C. Joshi, W. Lu, K. A. Marsh, W. B. Mori, P. Muggli, N. Vafaei-Najafabadi, D. Walz, G. White, Z. Wu, V. Yakimenko, and G. Yocky, Nature **515**, 92 (2014).

[21]I. Blumenfeld, C. E. Clayton, F.-J. Decker, M. J. Hogan, C. Huang, R. Ischebeck, R. Iverson, C. Joshi, T. Katsouleas, N. Kirby, W. Lu, K. A. Marsh, W. B. Mori, P. Muggli, E. Oz, R. H. Siemann, D. Walz, and M. Zhou, Nature **445**, 741 (2007).

[22]G. Xia, R. Assmann, R. A. Fonseca, C. Huang, W. Mori, L. O. Silva, J. Vieira, F. Zimmermann, and P. Muggli, J. Plasma Phys. **78**, 347 (2012).

[23]E. Gschwendtner, E. Adli, L. Amorim, R. Apsimon, R. Assmann, A. M. Bachmann, F. Batsch, J. Bauche, V. K. Berglyd Olsen, M. Bernardini, R. Bingham, B. Biskup, T. Bohl, C. Bracco, P. N. Burrows, G. Burt, B. Buttenschön, A. Butterworth, A. Caldwell, M. Cascella, E. Chevallay, S. Cipiccia, H. Damerau, L. Deacon, P. Dirksen, S. Doebert, U. Dorda, J. Farmer, V. Fedosseev, E. Feldbaumer, R. Fiorito, R. Fonseca, F. Friebel, A. A. Gorn, O. Grulke, J. Hansen, C. Hessler, W. Hofle, J. Holloway, M. Hüther, D. Jaroszynski, L. Jensen, S. Jolly, A. Joulaei, M. Kasim, F. Keeble, Y. Li, S. Liu, N. Lopes, K. V.

Lotov, S. Mandry, R. Martorelli, M. Martyanov, S. Mazzoni, O. Mete, V. A. Minakov, J. Mitchell, J. Moody, P. Muggli, Z. Najmudin, P. Norreys, E. Öz, A. Pardons, K. Pepitone, A. Petrenko, G. Plyushchev, A. Pukhov, K. Rieger, H. Ruhl, F. Salveter, N. Savard, J. Schmidt, A. Seryi, E. Shaposhnikova, Z. M. Sheng, P. Sherwood, L. Silva, L. Soby, A. P. Sosedkin, R. I. Spitsyn, R. Trines, P. V. Tuev, M. Turner, V. Verzilov, J. Vieira, H. Vincke, Y. Wei, C. P. Welsch, M. Wing, G. Xia, and H. Zhang, Nuclear Instruments and Methods in Physics Research Section A: Accelerators, Spectrometers, Detectors and Associated Equipment 2nd European Advanced Accelerator Concepts Workshop - EAAC 2015, **829**, 76 (2016).

[24]A. Caldwell, K. Lotov, A. Pukhov, and F. Simon, Nat Phys **5**, 363 (2009).

[25]K. V. Lotov, Phys. Rev. ST Accel. Beams **13**, 041301 (2010).

[26]C. Lechte, J. Stöber, and U. Stroth, Phys Plasmas **9**, 2839 (2002).

[27]F. F. Chen, Plasma Phys Control Fusion **33**, 339 (1991).

[28]A. W. Molvik, T. D. Rognlien, J. A. Byers, R. H. Cohen, A. R. Ellingboe, E. B. Hooper, H. S. McLean, B. W. Stallard, and P. A. Vitello, J Vac Sci Technol A **14**, 984 (1996).

[29]F. F. Chen and D. D. Blackwell, Phys Rev Lett **82**, 2677 (1999).

[30]A. W. Molvik, Phys Rev Lett **86**, 6048 (2001).

[31]G. G. Borg and R. W. Boswell, Phys Plasmas **5**, 564 (1998).

[32]D. D. Blackwell, T. G. Madziwa, D. Arnush, and F. F. Chen, Phys Rev Lett **88**, 145002 (2002).

[33]S. Cho, Physics of Plasmas **7**, 417 (2000).

[34]R. W. Boswell, Plasma Phys Control Fusion **26**, 1147 (1984).

[35]A. Komori, T. Shoji, K. Miyamoto, J. Kawai, and Y. Kawai, Phys Fluids B **3**, 893 (1991).

[36]Y. Sakawa, N. Koshikawa, and T. Shoji, Appl Phys Lett **69**, 1695 (1996).

[37]D. G. Miljak and F. F. Chen, Plasma Sources Sci Technol **7**, 537 (1998).

[38]S. Shinohara, T. Hada, T. Motomura, K. Tanaka, and T. Tanikawa, Phys Plasmas **16**, 057104 (2009).

[39]S. Shinohara, T. Motomura, K. Tanaka, T. Tanikawa, and K. P. Shamrai, Plasma Sources Sci Technol **19**, 034018 (2010).

[40]J. P. Squire, F. R. Chang Díaz, T. W. Glover, V. T. Jacobson, G. E. McCaskill, D. S. Winter, F. W. Baity, M. D. Carter, and R. W. Goulding, Thin Solid Films **506–507**, 579 (2006).

[41]A. M. Keesee and E. E. Scime, Plasma Sources Sci. Technol. **16**, 742 (2007).

[42]A. Degeling, N. Mikhelson, R. Boswell, and N. Sadeghi, Phys Plasmas **5**, 572 (1998).

[43]C. M. Denning, M. Wiebold, and J. E. Scharer, Phys Plasmas **15**, 072115 (2008).

[44]Y. Mori, H. Nakashima, F. W. Baity, R. W. Goulding, M. D. Carter, and D. O. Sparks, Plasma Sources Sci Technol **13**, 424 (2004).

[45]J. G. Kwak, H. D. Choi, H. I. Bak, S. Cho, J. G. Bak, and S. K. Kim, Physics of Plasmas **4**, 1463 (1997).

[46]G. R. Tynan, M. J. Burin, C. Holland, G. Antar, N. Crocker, and P. H. Diamond, Phys Plasmas **11**, 5195 (2004).

[47]F. F. Chen, Laser Part Beams **7**, 551 (1989).

[48]S. Shinohara, Y. Miyauchi, and Y. Kawai, Plasma Phys Control Fusion **37**, 1015 (1995).

[49]C. M. Franck, O. Grulke, and T. Klinger, Phys Plasmas **10**, 323 (2003).

[50]L. Liard, A. Aanesland, and P. Chabert, J Phys Appl Phys **45**, 235201 (2012).

[51]R. M. Magee, M. E. Galante, J. C. Jr, G. Lusk, D. W. McCarren, and E. E. Scime, Phys. Plasmas 1994-Present **20**, 123511 (2013).

[52]R. W. Boswell and R. K. Porteous, Appl. Phys. Lett. **50**, 1130 (1987).

[53]J. Gilland, R. Breun, and N. Hershkowitz, Plasma Sources Sci. Technol. **7**, 416 (1998).

[54]K. Takahashi, Y. Takao, and A. Ando, Appl. Phys. Lett. **108**, 074103 (2016).

[55]J. G. Kwak, S. K. Kim, and S. Cho, Physics Letters A **267**, 384 (2000).

[56]J. L. Kline, E. E. Scime, R. F. Boivin, A. M. Keesee, X. Sun, and V. S. Mikhailenko, Phys. Rev. Lett. **88**, 195002 (2002).